Journal of Hydrology 587 (2020) 124931

Contents lists available at ScienceDirect

Journal of Hydrology

journal homepage: www.elsevier.com/locate/jhydrol

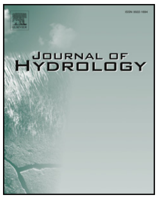

Research papers

# Mapping increases in hyporheic exchange from channel-spanning logjams

M. Doughty[a,*], A.H. Sawyer[b], E. Wohl[c], K. Singha[a]

[a] Hydrologic Science and Engineering Program, Colorado School of Mines, Golden, CO, United States
[b] School of Earth Sciences, The Ohio State University, Columbus, OH, United States
[c] Department of Geosciences, Colorado State University, Fort Collins, CO, United States

ARTICLE INFO

This manuscript was handled by marco borga, with the assistance of Francesco Comiti, Associate Editor

*Keywords:*
Hyporheic exchange
Logjam
Geomorphology
Electrical resistivity
MODFLOW
MT3DMS

ABSTRACT

Human impacts such as timber harvesting, channel engineering, beaver removal, and urbanization alter the physical and chemical characteristics of streams. These anthropogenic changes have reduced the number of fallen trees and amount of loose wood that form blockages in streams. Logjams increase hydraulic resistance and create hydraulic head gradients along the streambed that drive groundwater-surface water exchange. Here, we quantify changes in hyporheic exchange flow (HEF) due to a channel-spanning logjam using field measurements and numerical modeling in MODFLOW and MT3DMS. Electrical resistivity (ER) imaging was used to monitor the transport of solutes into the hyporheic zone during a series of in-stream tracer tests supplemented by in-stream monitoring. We conducted experiments in two reaches in Little Beaver Creek, Colorado (USA): one with a single, channel-spanning logjam and the second at a control reach with no logjams. Our results show that 1) higher HEF occurred at the reach with a logjam, 2) logjams created complex HEF pathways that caused bimodal solute breakthrough behavior downstream, and 3) higher discharge rates associated with spring snowmelt increased the extent and magnitude of HEF. Our numerical modeling supported all three field findings, and also suggested that lower flows increased solute retention in streams, although this last conclusion was not supported by field results. This study represents the first use of ER to explore HEF around a naturally occurring logjam over different stream discharges, and has implications for understanding how logjams influence the transport of solutes, the health of stream ecosystems, and stream restoration and conservation efforts.

## 1. Introduction

Surface water that moves into the alluvium via downwelling and then returns to the river farther downstream via upwelling defines hyporheic exchange flow (HEF; Tonina and Buffington, 2009). HEF has a substantial influence on a stream's ecosystem because it transfers dissolved oxygen, solutes, and nutrients into the subsurface and buffers stream-temperature fluctuations (e.g., Fanelli and Lautz, 2008). HEF thus improves water quality, regulates stream temperature, and maintains hospitable habitats for microorganisms and macroinvertebrates (e.g., Tonina and Buffington, 2009). The extent and magnitude of HEF are driven by surface and subsurface head distributions, which are controlled by geomorphic and hydrologic conditions in streams and rivers (Gooseff et al., 2006) including streambed heterogeneity in hydraulic conductivity (Salehin et al., 2004), stream meanders, bedforms (e.g., Cardenas et al., 2004; Hester and Doyle, 2008), changes in discharge (Wroblicky et al., 1998; Tonina and Buffington, 2011), and bed topography (Harvey and Bencala, 1993). Stream discharge generally increases HEF during snowmelt flows (Lautz et al., 2006; Loheide and Lundquist, 2009).

Logjams are an important aspect in river systems and impact stream geomorphology, hydrology, and ecology (e.g., Millington and Sear, 2007). Logjam hydrologic impacts increase as more of the flow is obstructed (Hester and Doyle, 2008; Sawyer et al., 2011). Benefits of logjams include increased channel complexity from the formation of anabranching channels, increased connectivity with the floodplain, control of downstream fluxes, storage of sediment and organic material, and enhanced habitat diversity (e.g., Livers and Wohl, 2016; Palmer et al., 2010; Sear et al., 2010). Logjams create hydraulic head variations along the river's flow path (e.g., Buffington and Tonina, 2009; Manners et al., 2007; Sawyer et al., 2011), increasing the hydraulic resistance and driving groundwater-surface water exchange (e.g., Buffington and Tonina, 2009; Wondzell, 2006). They also alter the thickness and grain-size distribution of alluvial bed substrate (Nakamura and Swanson, 1993) and promote development of bedforms, which drive downwelling and upwelling (Buffington and Tonina, 2009). Logjams therefore contribute to forming many of the conditions conducive for HEF (Lautz et al., 2006).

---

* Corresponding author.
*E-mail address:* megan.jean.colorado@gmail.com (M. Doughty).

https://doi.org/10.1016/j.jhydrol.2020.124931
Received 11 December 2019; Accepted 4 April 2020
Available online 07 April 2020
0022-1694/ Published by Elsevier B.V.

Despite its likely importance, the role of in-stream wood on HEF is not particularly well studied. Artificial logjams have been used in restoration efforts to counteract the effects of human impacts (Kail et al., 2007), although there has been little quantitative basis for their placement (Roni et al., 2014). Several studies have examined HEF around simple large-wood structures such as idealized single channel-spanning logjams or debris dams in field or flume experiments. For example, past studies have looked at the effects of wood addition on HEF using in-stream pressure measurements and temperature sensors in the field (Sawyer and Cardenas, 2012) or temperature changes in a flume (Sawyer et al., 2012). HEF rates have been found to be highest near single-log structures and decrease exponentially with distance upstream and downstream (Sawyer et al., 2011). Tracer experiments have also been used to quantify HEF in flume experiments to characterize hydraulic jumps from obstructions (Endreny et al., 2011) and in field experiments to examine debris dams in meadow streams (Lautz et al., 2006). Despite these advances in understanding HEF associated with large-wood structures, many of the existing studies are focused on relatively simple artificial and natural structures.

Yet we know the large wood impacts many natural stream systems, and likely their HEF. Human-driven impacts such as flow regulation, land-cover changes, and channel engineering—including removal of large wood—alter HEF by impacting sediment dynamics, bed substrate, channel morphology, and channel-floodplain connectivity (e.g., Campbell and Doeg, 1989; Poff et al., 2007; Wohl, 2005; Wohl and Beckman, 2014), resulting in cascading effects on hyporheic invertebrates (Hancock, 2002) and water temperature and chemistry (e.g., Allan, 2004; Sweeney and Newbold, 2014). Mountain streams, which provide vital aquatic habitats and retain and transmit essential nutrients and sediments downstream, have been particularly altered by land-use, as well as climate change (e.g., Wohl, 2006; Bernhardt and Palmer, 2007). Historically, a common method for "improving" these streams was to clear channels of obstructions such as boulders, leaning trees, or sunken logs to allow for easier timber conveyance and transportation (Sedell et al., 1991). The Front Range rivers of the Colorado Rocky Mountains have experienced 200 years of human alterations and provide an example of the resulting compromised river functions (Wohl, 2005).

Here, we focus on quantifying HEF in response to a natural channel-spanning logjam, which blocks large portions of the channel cross-section at different stream discharges. We examined two reaches of a partially confined mountain stream (Little Beaver Creek, Colorado USA) with and without a channel-spanning logjam by conducting tracer tests under varying flows using both in-stream monitoring and geophysical methods. We expected that HEF would increase in a reach with a logjam relative to a similar reach with no jam, and also that HEF would increase during peak snowmelt, regardless of jams, but would increase more in the reach with a logjam. To explore these expected behaviors, we performed tracer tests at the reaches of interest using dissolved NaCl as a conservative solute. NaCl is electrically conductive, which allows it to be visible to electrical resistivity (ER), which we use here, for the first time, to characterize changes in HEF due to logjams. Numerical modeling, using MODFLOW and MT3DMS, provided a simplified but valuable framework for understanding generalized solute transport behavior around a logjam in a steep mountain stream and therefore allowed for additional insight beyond the field measurements and helped to quantify the relations between logjams and HEF.

## 2. Methods

### 2.1. Site observations

We measured HEF along two segments of Little Beaver Creek, a third-order tributary to the South Fork of the Cache la Poudre River in northern Colorado (Fig. 1A and B). We chose this site because there has been previous work on logjam characteristics (Jackson and Wohl, 2015), the stream has had little to no human impact, and there are reaches with different levels of logjam complexity. We chose two reaches for our work: one with a single, channel-spanning logjam and long enough to conduct a well-mixed tracer test, and another reach without a logjam to serve as a control. Channel width in both reaches averages 6 m and channel gradient averages 0.02 m/m. The surrounding montane forest is dominated by Ponderosa pine (*Pinus ponderosa*) and the riparian zone contains Ponderosa pine, Douglas-fir (*Pseudotsuga menziesii*), Engelmann spruce (*Picea engelmannii*), and aspen (*Populus tremuloides*). The watershed (40 km$^2$ drainage area) is at 1830–2740 m elevation and flow is snowmelt dominated. While spring runoff and summer floods can move large-wood pieces and sometimes remove logjams, the jams at this site have remained relatively constant from year to year based on our observations. Average valley width increases downstream in the study area and wood load in the channel decreases (Ader, 2019). Ground-penetrating radar data suggest that the depth to bedrock is approximately 1 m and increases in average depth (~2–3 m) and variability in the lower portion of the study area (Dan McGrath, personal communication, October 9, 2018).

The logjam site includes one channel-spanning logjam (Fig. 1D). A single tree makes up the key piece of the jam with other loose wood and organic material built up behind and around it. Looking immediately downstream, the right bank of the site is highly vegetated with moist soils as well as some standing water, particularly during high flows. The left bank is steeper with less vegetation. The control transect has no logjams within the reach (Fig. 1C), but is downstream of the logjam reach; this was the only viable reach with a long enough stretch without logjams to expect complete mixing of the tracer. Both banks at this transect are highly vegetated, with slightly more vegetation on the left bank. An abandoned beaver dam and inactive channel were observed approximately 100 m across the floodplain from the left bank of the control transect.

### 2.2. Tracer injection

We conducted three constant-rate injections of dissolved NaCl for 4 h upstream of the logjam and control sites (Fig. 1; Table 1). The tracer was pumped into Little Beaver Creek at the injection site (Fig. 1) at a low flow rate relative to stream discharge while in-stream and ER measurements were continuously collected. The first tracer test was conducted in June during peak snowmelt runoff, while the second and third tests were performed in July under similar, lower flows (Table 1). For each test, the tracer was injected at a single location and constant rate from well-mixed reservoirs of constant concentration. More mass was injected during the higher flow in order to increase the in-stream fluid conductivity by approximately 50 uS/cm for all three tests (Table 1). The injection sites were approximately 50 and 250 m upstream, respectively, of the two monitored sites to allow the tracer to mix fully into the stream. The stream was monitored before the tracer test and for a minimum of 24 h after injection using in-stream fluid EC transducers above the injection site and above and below the monitored sites (Fig. 1). There were thunderstorms on July 28 and 29 that affect some results, as outlined below.

### 2.3. Electrical resistivity imaging

Tracer tests are often interpreted for HEF or transient storage residence times using solute breakthrough curves (BTCs) from the stream or well networks (e.g., Wörman et al., 2002; Anderson et al., 2005; Lautz et al., 2006; Wondzell, 2006; Tonina and Buffington, 2007), but these spatially sparse measurements often limit our ability to map heterogeneity in HEF. In contrast, electrical resistivity (ER) provides spatially rich data on the subsurface bulk electrical conductivity, which is sensitive to porosity, total dissolved solids, and geologic material, and has often been used to characterize groundwater-surface water interactions (e.g., Singha et al., 2010; Slater et al., 2010; Cardenas and

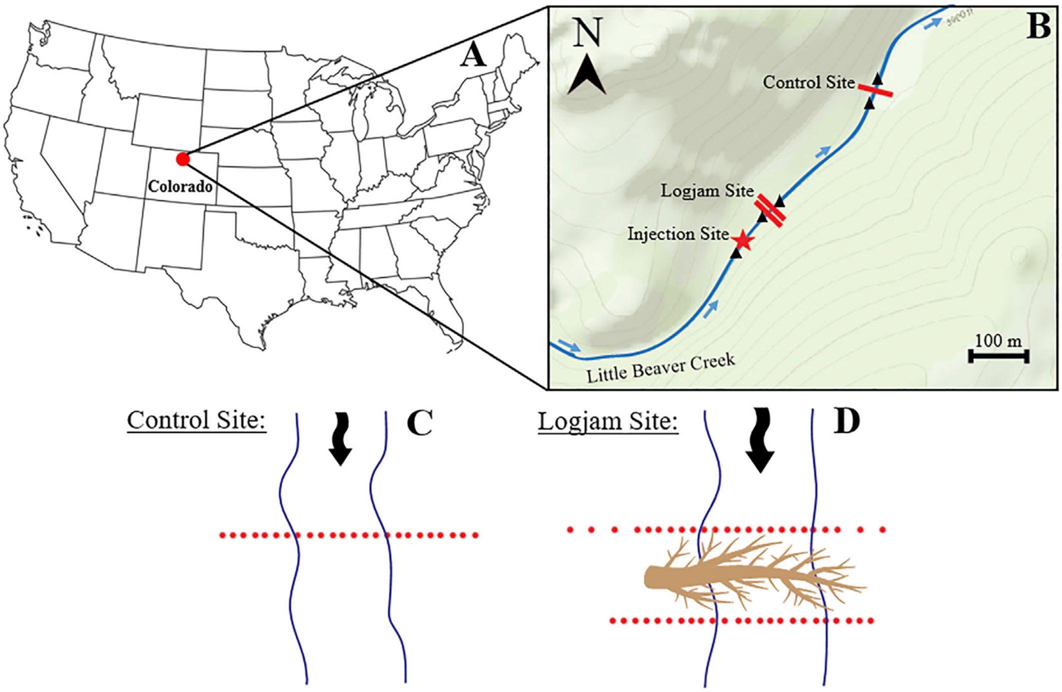

**Fig. 1.** (A) Location of Little Beaver Creek, Colorado (40.62, −105.54). (B) The inset map shows the location of the injection site (red star) relative to the three ER transects (red lines) and the five in-stream fluid electrical conductivity monitoring sites (black triangles) at the logjam and control transects. The ER transects indicated on this map are not to scale. (C-D) Map views of the ER lines at the control site (C) and the logjam site (D) and associated electrodes (represented by the red dots) perpendicular to the stream.

Markowski, 2011; Coscia et al., 2011).

ER is a direct-current method that passes low-frequency alternating current through a pair of electrodes, which are placed into the ground. The subsequent voltage is measured in another two electrodes. This process proceeds using different combinations of electrodes, allowing collection of hundreds of measurements in minutes. The injection of a highly conductive fluid, such as dissolved NaCl, increases the bulk conductivity of the subsurface, so ER measurements can provide a multidimensional look at subsurface transport through time, and consequently serve as a useful supplement to point-based fluid EC BTCs (Ward et al., 2010a, 2010b; Toran et al., 2013; Ward et al., 2014). In a time-lapse inversion, the background conditions are differenced from the images, making ER a valuable method for characterizing hydrologic processes in the natural environment (Ward et al., 2010b; Cardenas and Markowski, 2011; Coscia et al., 2011) or stream restoration structures (Toran et al., 2012; Toran et al., 2013).

ER data were collected using an IRIS Syscal Pro Resistivity Meter, using a dipole–dipole geometry and 24 electrodes per line with 0.5- to 1-m spacing (Fig. 1C, D), collecting 231 measurements per time step. The survey times for the transects were approximately 8 min long, which allowed for high temporal resolution data of the tracer transport. Three total transects were monitored during the three tracer tests: two were located above and below the logjam being monitored and the third was located at the control transect (Fig. 1B). Background ER data were collected for a minimum of 1 h before the injection began along the transects. Data collection continued during and then after the 4-hour tracer injection for at least 24 h to monitor the tracer entering and leaving the subsurface. During data collection, two replicate measurements were collected and averaged. The mean standard deviation across replicate measurements was 0.23%.

The bulk apparent conductivity, $\sigma_a$, was calculated from the measured resistance data ($V/I$) using equation (1) and the geometric factor, $K$, in equation (2), which accounts for the arrangement of electrodes:

$$\sigma_a = \frac{I}{VK} \tag{1}$$

$$K = \frac{2\pi}{\frac{1}{AM} - \frac{1}{AN} - \frac{1}{BM} + \frac{1}{BN}} \tag{2}$$

where $I$ is the current injected into the ground (amperes), $V$ is the voltage measured (volts), $A$ and $B$ are the current electrodes, and $M$ and $N$ are the potential electrodes that the resistivity meter uses. To compare the BTCs from the in-stream monitoring to the ER data, we averaged the calculated bulk apparent conductivity along the entire transect to create a composite "breakthrough curve" for the entire transect.

ER methods are sensitive to temperature changes in the subsurface (Hayley et al., 2007; Hayley et al., 2010). Therefore, iButton temperature stakes were installed to measure the temperature every 10 min at 10 cm and 40 cm below the ground surface near the logjam transects and the control transect. The temperature stake at the logjam site also had an iButton at the surface to measure air temperature fluctuations.

**Table 1**
Details of tracer tests. Stream discharge was measured using stream gauging and a stilling well. Mean tracer EC is measured inside of the injection tubs before injection into the stream.

| | Stream discharge ($m^3/s$) | Background Stream EC (uS/cm) | Tracer Injection Rate ($m^3/s$) | Mean Tracer EC (mS/cm) | Total Mass of Tracer Injected (kg) |
|---|---|---|---|---|---|
| June 13–14, 2018 | 0.76 | 15.8 | $1.2 \times 10^{-4}$ | 228.1 | 318 |
| July 10–11, 2018 | 0.17 | 21.6 | $3.0 \times 10^{-5}$ | 240.8 | 91 |
| July 28–29, 2018 | 0.18 | 24.9 | $2.1 \times 10^{-5}$ | 242.5 | 79 |

### 2.4. Inversion of ER data

Resistance data were inverted using the code R2 (v 3.1), an inverse model accounting for 3-D current flow based on Occam's solution, as described by Binley and Kemna (2005). All four boundary conditions of the 2-D mesh are zero flux and the boundaries are set a substantial distance, approximately 130 m, from the area of investigation. A time-lapse inversion was used, which calculates the percent difference from the background data such that errors related to field configuration and discretization are minimized (LaBrecque and Yang, 2009). Inversions from background measurements were used as the starting model for all data collected.

The resolution matrix was also calculated; this shows how well each model parameter is resolved given the ER data in the last iteration of the inversion. Multiple factors affect the calculation of the resolution matrix, including electrode layout, measurement scheme, data signal-to-noise ratio, bulk electrical conductivity distribution, and the parameterization and regularization used in the inversion (Binley and Kemna, 2005). The equation for the resolution matrix (e.g., Binley and Kemna, 2005) is as follows:

$$R = (J_k^T W_d^T W_d J_k + \alpha W_m^T W_m)^{-1} J_k^T W_d^T W_d J_k \tag{3}$$

where $k$ is the final inversion iteration, $T$ is the transpose operator, $d$ is the data, $J_k$ is the Jacobian matrix for the current model $m$, $W_d$ is the data weighting matrix associated with individual data errors, $W_m$ is the model weighting matrix, and $\alpha$ is the regularization parameter. Values on the diagonal of the $R$ matrix close to 1 indicate that the parameter was resolved perfectly. As the values decrease, the resolution does as well. Values near zero indicate parameters that cannot be uniquely resolved. In general, resolution decreases with distance and depth from the electrodes.

### 2.5. Numerical modeling of flow and transport

The flow and transport of an idealized, straight channel and stream corridor were modeled to explore potential changes in HEF due to changes in stream flow and logjams (Fig. 2). These models were not calibrated because the goal is not to predict the exact behavior of solute transport in the field, where the hydrology and geology are particularly complex, but rather to elucidate and support the general observations from ER inversions, which are subject to constraints from resolution, inversion artifacts, and other challenges. The steady-state groundwater flow model was built using MODFLOW (Harbaugh, 2005), and transient solute transport was modeled using MT3DMS (Zheng and Wang, 1999) to simulate tracer injections. We used a steady-state groundwater model because we were not looking at event-based changes, but seasonal changes. Over the time that our tracer tests were being conducted, the changes in discharge were nominal.

We explored four model configurations: 1) no logjam at high flow, 2) single logjam at high flow, 3) no logjam at low flow, and 4) single logjam at low flow. As in field experiments, the simulated tracer test is represented as a continuous injection for 4 h at fixed concentration. It is assumed that the tracer is conservative and nonreactive. These relatively simple, idealized models are intended to compliment and clarify results from ER imaging, not to recreate exact field conditions, which would have required more information on heterogeneity in subsurface geology and hydraulic heads created by current interactions with the bed than existed. We also were not trying to characterize this site only, but to develop intuition on processes that could be extrapolated to other sites. We therefore do not directly compare measured and modeled BTCs, but only their relative differences.

The model domain consists of three homogeneous, isotropic material types intended to represent soil, alluvium, and bedrock, loosely based on the field system and other mountain streams on the Colorado Front Range (Fig. 2; Table 2). The soil layer is 1 m deep and has a relatively high hydraulic conductivity (8 m/d). The stream lies within the soil layer and is 0.9 m deep and 1 m wide (Fig. 2B). The elevation of the top of the stream cells (water surface) is 0.1 m lower in elevation than the surrounding material in the upper layer (land surface). Under the soil, the alluvium (Table 2) is 5 m thick and has a 1 m discretization. The bottom layer, which represents fractured bedrock, is 5 m thick (Table 2). The entire domain is 70 m in the downstream direction (X), 30 m in the cross-valley direction (Y), and 11 m in the vertical (Z). Cell sizes are 1 m (in X, Y, and Z) in the first two layers and increase to 1 by 1 by 5 m (in X, Y, and Z) in the third layer. We kept heterogeneity relatively simple within the model as we looked to simulate a system transferable to other headwater mountain streams, with shallow soils overlying regolith and then bedrock.

The stream and logjam, located within the top model layer, were treated as equivalent porous media (Table 2). This approach has been used in previous surface water-groundwater exchange models (Mao et al., 2006; Robinson et al., 2007) and was adopted because stream and river packages in MODFLOW and MT3DMS do not represent lateral exchange flows between the stream and aquifer (Ben Simon et al., 2015). Along the stream surface, hydraulic head was set to vary under high-flow scenarios from 13.8 m at the top of the reach to 11 m at the bottom, leading to an overall hydraulic gradient of 0.02. Under low-flow scenarios, head varied from 11.7 to 11 m, leading to a lower gradient of 0.01. Using a high hydraulic conductivity stream also allows the inclusion of the logjam as a porous medium in the stream system that alters the head distribution near the sediment–water interface. Because the effective hydraulic conductivities of logjams are not widely known, we calculated a value using Darcy's law and the discharge from the no-logjam numerical model, where the cross-sectional area (A) was of the modeled stream (0.9 $m^2$) and the desired head drop (dh) was 0.5 m across a 1 m distance (dL).

The upstream and downstream sides of the model were set to constant head values equal to the head at the upstream and downstream ends of the channel. The other model sides, top, and bottom were defined as no-flow boundaries. All no-flow boundaries were defined as zero mass-flux boundaries in the transport model and the constant-head boundaries were given a concentration of 0 in MT3DMS, with the exception of the inlet face of the stream cell where concentration was varied over time to represent the injection. The transient solute transport model spanned 100 days. Initially, concentration throughout the domain was set to 0 mg/L, and the upstream cell of the channel (at the constant-head boundary) was specified with a concentration of 100 mg/L for 4 h, followed by 0 mg/L.

To compare the four model configurations, we examined concentration BTCs at the three transects along the synthetic stream corresponding to our field transects: transect A (above the logjam, when it existed), transect B (below the logjam, when it existed), and transect C (a downstream control from A and) (Fig. 2). At each transect, we explored the tracer response at three locations in the subsurface (1 m and 2 m below the stream, and 2 m lateral to the stream) for each transect (Fig. 2). Temporal moments were calculated for the nine BTCs (the three cells at each of the three transects; see Section 2.6) to analyze the movement of the tracer and assess the effect of the logjams at varying flow rates. In addition to the BTCs, we analyzed the water flux into and out of the stream to characterize and compare the amount of HEF among the models.

### 2.6. Temporal moments

To look at how controlling processes vary with discharge and the presence/absence of a logjam, we analyzed the following moments of solute BTCs from field measurements (both surface and subsurface water) and models (subsurface only): mass, mean arrival time, variance, and skew (Gupta and Cvetkovic, 2000; Harvey and Gorelick, 1995). The moments analyzed from the subsurface in the field were based off the bulk apparent conductivity BTCs from ER for qualitative comparison to

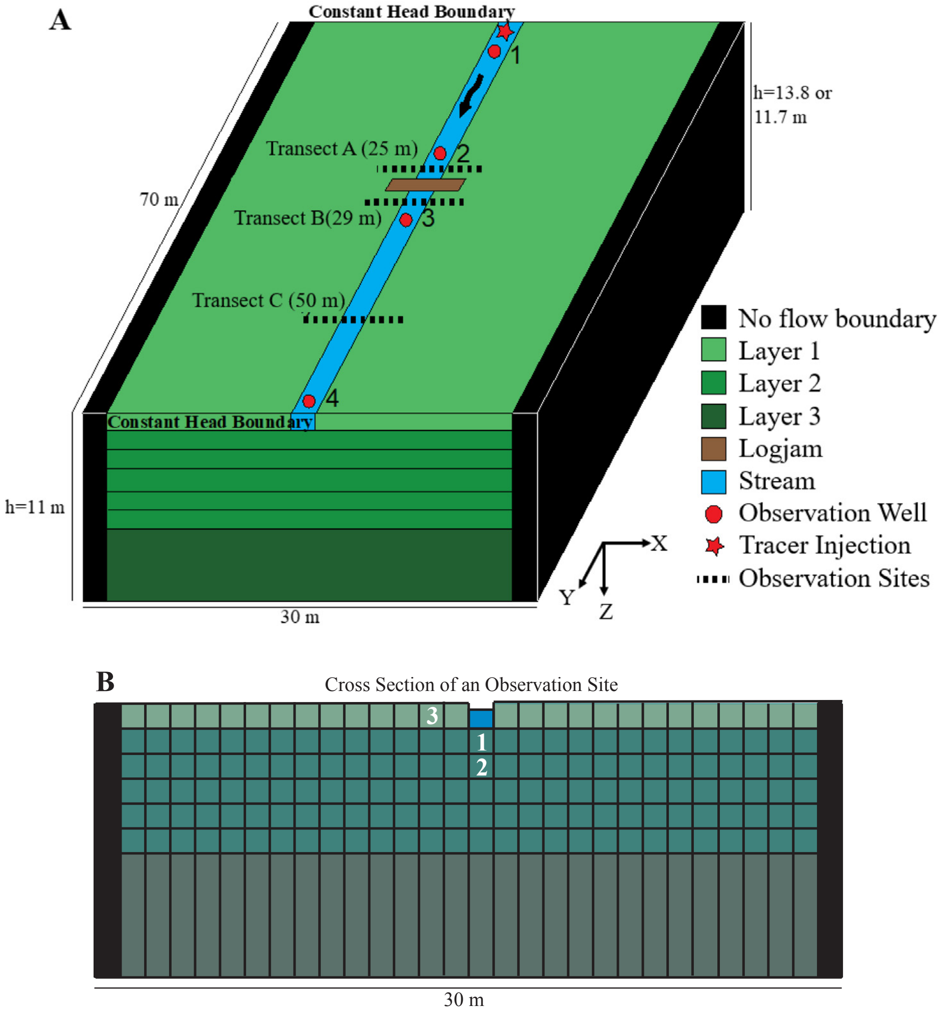

**Fig. 2.** (A) Flow and transport model setup, showing the subsurface, the stream, and the logjam (when present, at X = 27 m). The top constant-head boundary and elevation is 13.8 m for the high-flow and 11.7 m for the low-flow model. Transect A (above the logjam when it exists, X = 25 m), B (below the logjam when it exists, X = 29 m), and C (the downstream control, X = 50 m) are the observation transects where we determine solute BTCs at three cells, shown in (B) the cross section. Cell 1 is at Y = 15 m and Z = 2 m, cell 2 is at Y = 15 m and Z = 3 m, and cell 3 is at Y = 13 m and Z = 1 m.

one another (Ward et al., 2010a). Since each field tracer test was not monitored for exactly the same time interval, data were truncated so the same amount of time was used for the temporal moment calculations to prevent misrepresentations in the calculations. The n$^{th}$ order temporal moment ($M_n$) was calculated by:

$$M_n = \int_0^\infty t^n c(t) dt \tag{4}$$

$$c = EC * 0.5 \tag{5}$$

where $t$ is time, $n$ is the order of the moment, and $c(t)$ is concentration (mg/L) at time $t$. Concentration $c$ is assumed to be linearly related to total dissolved solids (mg/L) and $EC$ (uS/cm) (Keller and Frischknecht, 1966) (Equation (5)). To estimate moments, the background electrical conductivity was first removed from the data. The zeroth moment (mg*s/L) is the total tracer mass passing the observation point per unit of discharge. To find the total mass passing the observation point, the zeroth moment was multiplied by the average flow, which was done for both the in-stream and ER measurements. The mean arrival time ($\bar{t}$) of the injected tracer at the point of observation is calculated using:

$$\bar{t} = \frac{M_1}{M_0}. \tag{6}$$

The variance of the pulse describes the spread of the BTC and is related to the second, first, and zeroth temporal moments:

$$\sigma^2 = \frac{M_2}{M_0} - \left(\frac{M_1}{M_0}\right)^2. \tag{7}$$

The skewness of the data describes asymmetry of the BTC based on

**Table 2**
Model Properties. The stream is a linear feature within Layer 1.

| | Hydraulic Conductivity (m/d) | Porosity (-) | Thickness (m) | Dispersivity Longitudinal/Transverse (m) |
|---|---|---|---|---|
| Layer 1 (soil) | 8 | 0.3 | 1 | 0.1 / 0.01 |
| Layer 2 (alluvium) | 1 | 0.1 | 5 | 0.1 / 0.01 |
| Layer 3 (fractured bedrock) | 0.0005 | 0.5 | 5 | 0.1 / 0.01 |
| Logjam | 9028 | 0.6 | 1 | 0.1 / 0.01 |
| Stream | 100,000 | 0.9999 | 1 | 0.1 / 0.01 |

solute retention (Drummond et al., 2012). A more positive skewness ($\mu_3$) value indicates a larger degree of tailing behavior exhibited in the BTC, and therefore, a higher amount of hyporheic exchange:

$$\mu_3 = \frac{M_3}{M_0} - 3\sigma^2\frac{M_1}{M_0} - \left(\frac{M_1}{M_0}\right)^3. \tag{8}$$

## 3. Results

We begin by describing general differences in the observed fluid and average bulk apparent conductivity, as well as inverted bulk conductivity from the three transects from the field tracer experiments (above and below the logjam and the downstream control without a logjam). We then compare the field data with the behavior from the three transects in the numerical models, both with and without a logjam.

For all field data, there is a +/-3 uS/cm fluctuation in the background fluid conductivity values before the tracer injection. The fluid conductivity in the stream increases almost immediately after the tracer injection begins, “plateaus” during the injection around 90–100 uS/cm if the EC transducer was in the main flow path (with a slow decrease through the peak as a function of changing stream discharge and temperature), and returns to background almost immediately after the tracer tests end (Fig. 3, SI-3, and SI-4).

The average bulk apparent conductivities from ER show a slow increase during the tracer-injection plateau instead of the slight decrease in the fluid conductivity plateau as measured from EC transducers during the same time (Fig. 3, SI-3 and SI-4). This is likely due to the tracer dispersing throughout the course of the tracer test, so the tracer is then better resolved by the ER measurements (e.g., Bethune et al., 2015). The average bulk apparent conductivity does not return to background immediately like the fluid measurements at any flow rate. The temporal moments for the fluid and bulk apparent conductivities were calculated at each transect to demonstrate patterns and similarities across different flows and transect locations (Fig. 4).

The background ER inversions show similar patterns in subsurface bulk electrical conductivity for all three transects (Fig. 5A-C for the June 13–14 tests; SI-1A-C and SI-2A-C for the later two tests in July): conductive regions under the stream and near the surface where the sediments have higher porosity, and less conductive material deeper into the subsurface. All transects show low bulk conductivity about a half meter below the surface, which likely corresponds to the top of a cobble layer that we observed in the field. In the time-lapse inversions, regions with large increases in bulk conductivity are where the tracer moves through the subsurface (Fig. 5D-I, SI-1D-I, and SI-2D-I). Conversely, areas with little to no change in bulk conductivity are where little to no tracer is observed. The resolution matrices for all transects show high resolution along the surface to about 2 m deep from where the electrodes start and end (Fig. 5J-L, SI-1 J-L, and SI-2 J-L).

The maximum temperature variation at a depth of 10 cm was 3.5 °C at the control site and 2.5 °C at the logjam site at any time during the tracer tests and was 2 °C at the control site and 0.5 °C at the logjam site at 40 cm. For some of the tracer tests, no temperature changes were observed at a depth of 40 cm. Due to the small change in temperature throughout the ER observational periods, no temperature corrections were made to the bulk apparent conductivity or inversions.

### 3.1. Control transect measurements

The changes in inverted bulk conductivity for the control transect 1 h after the tracer injection started (Fig. 5D, SI-1D, SI-2D) show the tracer moving under the stream and into the left bank along the transect from 4 to 8 m at a depth from 0.5 to 1 m, regardless of stream flow rate. The left bank of the stream has a lower slope than the right and is also before a bend in the stream, which would favor hyporheic exchange through the left bank. There is a greater change in bulk apparent conductivity measurements from background during the June 13–14 tracer test compared to the two tests in July (Fig. 3A, SI-3A, SI-4A), which leads to the June tracer test having a larger area (estimated using the 200% change in bulk conductivity contour) compared to the two tests in July, suggesting a larger hyporheic extent. We do not calculate actual areas but just look at relative comparisons due to issues with out-of-plane effects in 2-D ER inversions (e.g., Ward et al., 2010a). It becomes difficult to image the tracer once the injection ends for all three tests as the percent changes in electrical conductivity from background start to fall within the data noise.

In the average bulk apparent conductivity data from this transect there is also a small secondary peak after the tracer ends and then a slow return to background on the receding limb for all tracer tests (Fig. 3A, SI-3A, SI-4A). This might be caused by the release of solutes from the logjam site located upstream. The mean arrival times based on the average bulk apparent conductivity are longer than those calculated from fluid conductivities (7–10 h vs. 2–3 h), increasing with lower flows (Fig. 4F). Based on stream discharge, it takes approximately 10 min for the tracer to reach the control from the injection point in the stream, but transport through the aquifer would be much slower. Variation in higher-order moments is shown in Fig. 4. Most notable is the decrease in skew with each tracer test through time.

### 3.2. Control transect models

The BTCs from the cell 1 m below the stream (at Y = 15 m, Z = 2 m) for the no-logjam, low-flow numerical model show that concentration increases rapidly after the start of the tracer, peaks, and

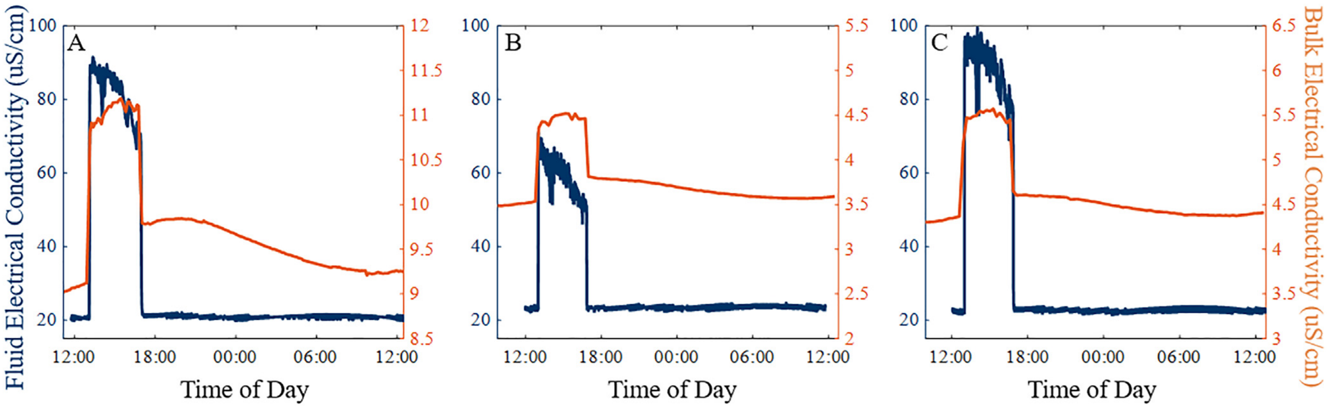

**Fig. 3.** Fluid and mean bulk apparent conductivity from the June 13–14 tracer test for the (A) control, (B) above-logjam, and (C) below-logjam sites. For comparison, results from the two July tests are shown in Figures SI-3 and SI-4.

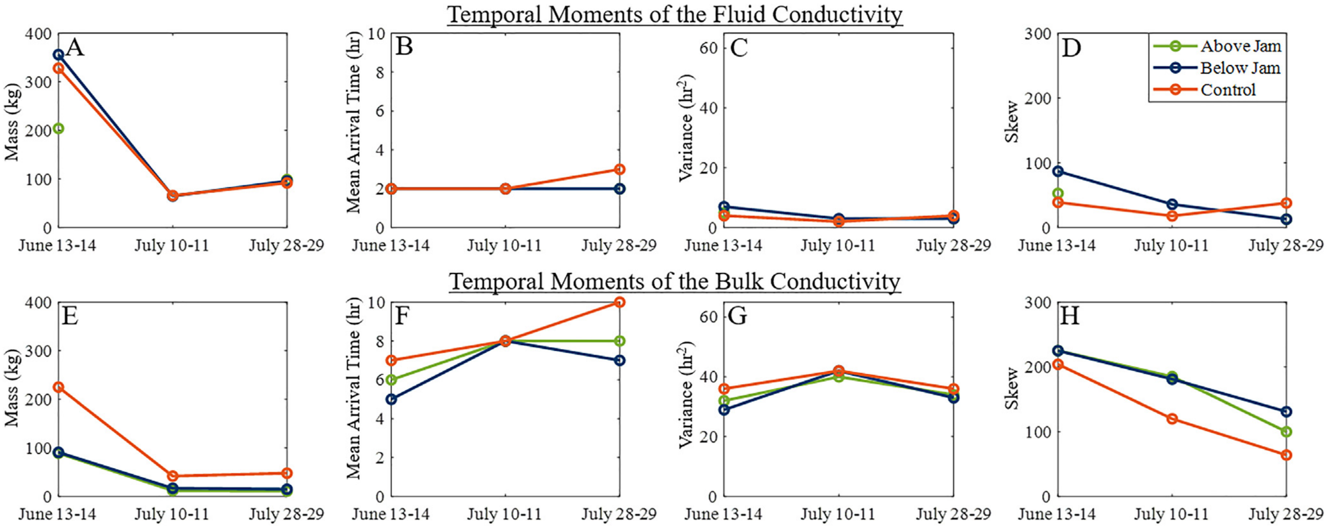

**Fig. 4.** Temporal moments (mass, mean arrival time, variance, and skew) estimated from the mean fluid apparent conductivity (A-D) and the mean of the bulk apparent conductivity (E-H) through time.

then decreases rapidly after the end of the tracer (Fig. 6A-C). The concentration at this cell drops more quickly after the tracer ends in the high-flow case (Fig. 6A-C). Because solute exchange beneath the channel is fairly uniform along the synthetic reach, the mass, mean arrival time, variance, and skew are similar at all three transects at both high and low flow for the cell 1 m below the stream (Fig. 7A-D).

Observed mass, mean arrival time, variance, and skew values 2 m lateral to the stream (at Y = 13 m, Z = 1 m) all increase downgradient, from Transect A to B to C at low flow (Fig. 7I-K). At high flows, the BTCs show similar behavior and low concentrations along the channel (Fig. 6G-I), so the mass, mean arrival time and variance remain relatively consistent at all three transects (Fig. 7I-L), with only slight increases downgradient from Transect A to B to C.

Little to no concentration is detected in any of the locations 2 m below the stream (at Y = 15 m, Z = 3 m; Fig. 6D-F) at high or low flows, so temporal moments are not calculated. Flow is primarily directed down-valley, and dispersion does not mix the tracer to 2 m depth over the timescale of simulations, despite losing conditions in the models without logjams (Fig. SI-5).

At low flows, the net water flux across the streambed (Table 3) is from the stream to the aquifer ($2 \times 10^{-5}$ m$^3$/s), and no regions of groundwater discharge to the stream occur. The rate of loss is influenced by the channel hydraulic head gradient, which was chosen to be similar to our field setting. The water flux across the streambed, integrated over the 70-m long model reach, is approximately 0.17% of the daily discharge in the modeled stream, which is within observations

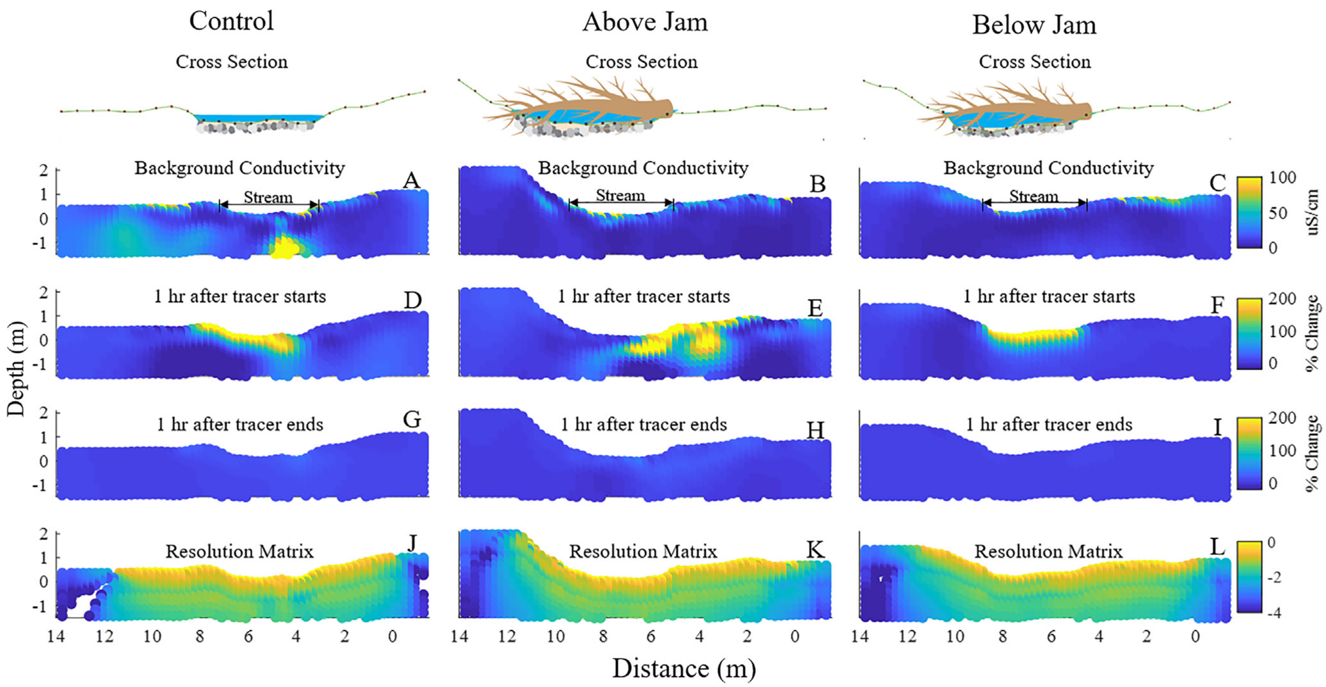

**Fig. 5.** ER results from the three transects, oriented looking downstream from the June 13–14 tracer test. A-C: background bulk conductivity along the three ER transects (background fluid conductivity of 23.2 uS/cm). D-F: changes in bulk conductivity 1 hr into the tracer injection. G-I: changes in bulk conductivity 1 hr after the tracer injection ended. J-L: log10(diagonal resolution matrix) of the three transects. Pixels close to 0 in log10 space have perfect resolution. The more negative a pixel in log space, the less perfect the resolution. For comparison, results from the two July tests are shown in Figures SI-1 and SI-2.

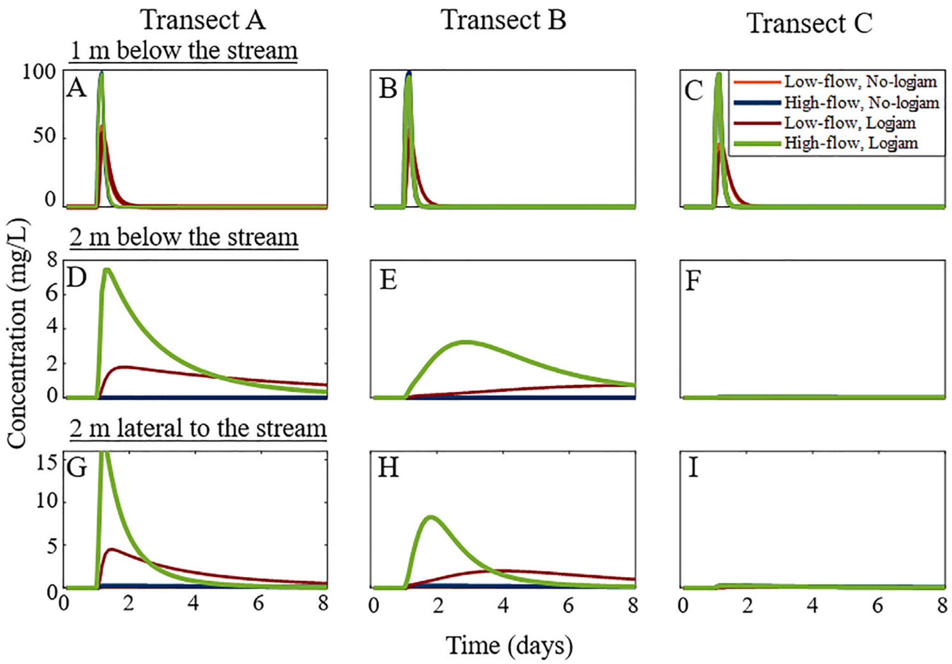

**Fig. 6.** Model concentrations (mg/L) for the three subsurface cells in the three transects (A, B, C) for the four model configurations. In models with jams, Transect A is immediately above the jam and B is immediately below (Fig. 2). (A-C) Concentrations 1 m below the stream (Y = 15 m, Z = 2 m). (D-F) Concentrations 2 m below the stream (Y = 15 m, Z = 3 m). (G-I) Concentrations 2 m lateral to the stream (Y = 13 m, Z = 1 m). Only the first 8 days of the 100-day monitoring period are shown.

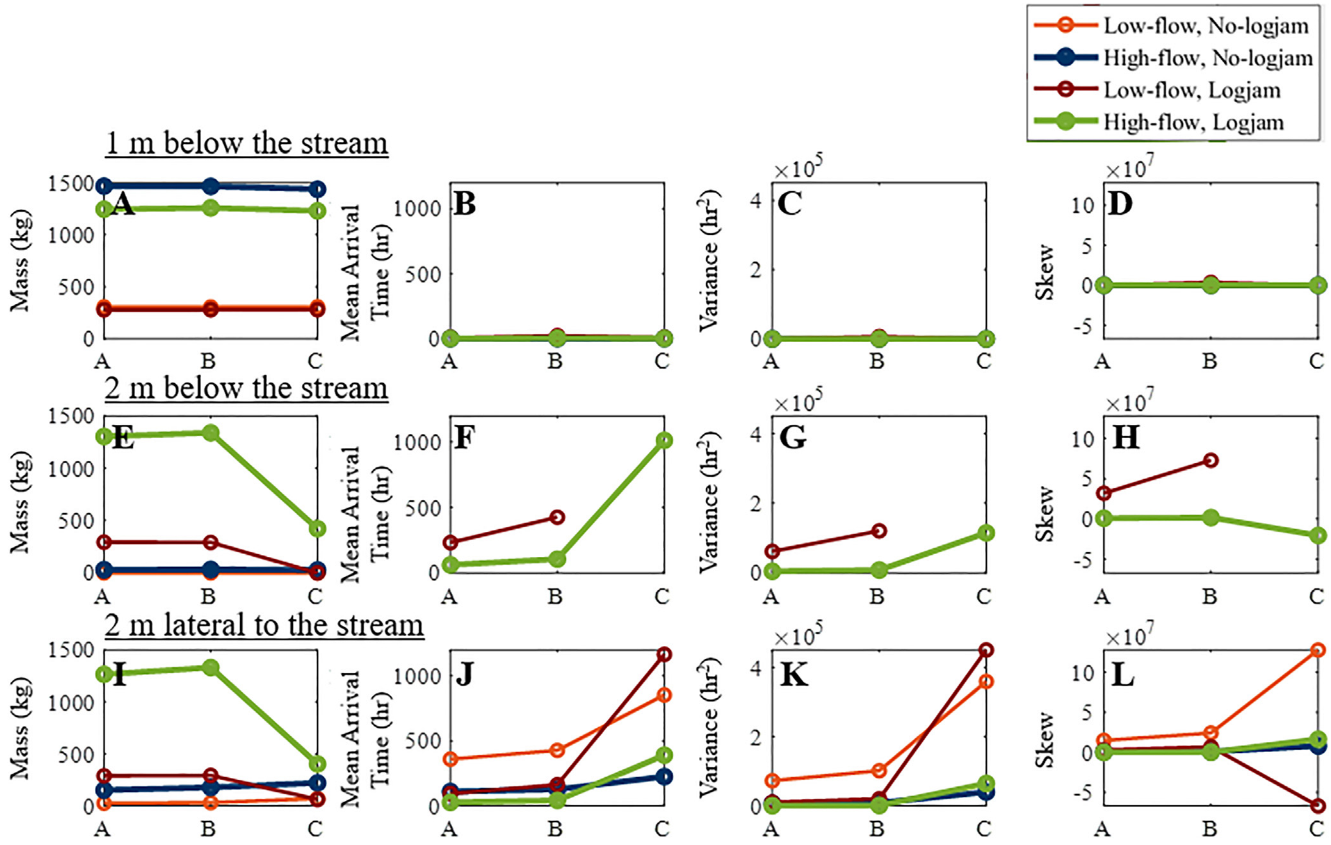

**Fig. 7.** Temporal moments for the modeled tracer tests. (A, E, I) Mass, (B,F, J) mean arrival time, (C, G, K) variance, and (D, H, L) skew values from the four model configurations for all three transects (labeled A-C on the x-axis), for the three cells considered: 1 m below the stream (A-D), 2 m below the stream (E-H), and 2 m lateral to the stream (I- L). No estimates exist for the low-flow, no-logjam and high-flow, no-logjam cases for some estimates due to low concentrations in the breakthrough curves.

from natural mountain streams in arid regions (e.g., Payn et al., 2009). At high flows, the model stream is losing a greater amount compared to the low-flow scenario (Table 3). Again, no regions of groundwater discharge to the stream occur. The rate loss integrated over the 70-m long model reach is approximately 0.15% of the model discharge for the high flow model.

### 3.3. Above the logjam measurements

The changes in inverted bulk conductivity during the tracer

**Table 3**
Surface water-groundwater exchange flows integrated across streambed cells from MODFLOW model.

| | Low-flow, no-logjam | High-flow, no-logjam | Low-flow, logjam | High-flow, logjam |
|---|---|---|---|---|
| Total stream discharge ($m^3/s$) | 0.01 | 0.04 | 0.01 | 0.03 |
| Inflow: aquifer to stream ($m^3/s$) | 0.0 | 0.0 | $1 \times 10^{-5}$ | $5 \times 10^{-5}$ |
| Outflow: stream to aquifer ($m^3/s$) | $2 \times 10^{-5}$ | $6 \times 10^{-5}$ | $3 \times 10^{-3}$ | $1 \times 10^{-4}$ |
| Net loss (out-in) ($m^3/s$) | $2 \times 10^{-5}$ | $6 \times 10^{-5}$ | $2 \times 10^{-5}$ | $7 \times 10^{-5}$ |

injection show the tracer moving through the subsurface of the less-steep right bank and partially under the stream at a depth from 0.5 to 2 m, along the transect from 4 to 9 m, for all flows (Fig. 5E, SI-1E, and SI-2E). As at the control, the tracer test from June 13–14 has a higher percent change in bulk conductivity than the other dates (Fig. 3B, SI-3B, SI-4B) and also shows the tracer moving at a greater depth compared to the July 10–11 and July 28–29 tests (Fig. 5E, SI-1E, SI-2E). Similarly, there is a larger area associated with the change in bulk apparent conductivity during the June 13–14 tracer test compared to the area calculated from the two tests in July.

The calculated tracer masses from the bulk apparent conductivity are consistently smaller than those at the control transect for both tests but have a similar magnitude to those calculated for the below-logjam transect (Fig. 4), described below. The mean arrival times estimated from mean bulk apparent conductivity (Fig. 4F) range from 6 to 8 h (longer than those of ~2 h estimated from the fluid conductivity), increasing for the two July tracer tests. The mean arrival times at this transect are about 1–2 h less than those estimated from the geophysics at the control transect, which is farther downgradient. The temporal variance tends to be slightly smaller for the logjam transects than the control (Fig. 4G), which would indicate less dispersion of the tracer at logjam sites. This makes sense given the downstream position of the control site compared to the logjam sites; this additional distance would allow more time for spreading of the tracer compared to the upstream logjam sites closer to the injection.

### 3.4. *Below the logjam*

The changes in inverted bulk conductivity one hour into the tracer injection (Fig. 5F, SI-1F, SI-2F) show the tracer moving almost solely under the stream at a depth of 0.5 to 1 m along the transect from 4 to 9 m for all three tracer tests. The July 10–11 test also shows the tracer moving a little deeper in the subsurface than the other two tests and toward the left bank, but the location of the tracer is otherwise largely similar between tests. The tracer is difficult to see even one hour after the end of injection (Fig. 5I, SI-1I, and SI-2I). As in the other transects, there is a larger change in bulk apparent conductivity from background during the June 13–14 tracer test than the two tests from July (Fig. 3C, SI-3C, SI-4C); consequently, the estimated area of tracer extent in the June 13–14 transects an hour into the tracer test is larger than the two July tests (Fig. 5F, SI-1F, SI-2F) as seen at the other two transects, indicating a potentially larger hyporheic zone with high flow.

The drop in average bulk apparent conductivity after the injection ends is more gradual during the July 28–29 test (Fig. 3C, SI-3C, SI-4C), but this is likely due to gaps in data caused by the thunderstorms. The temporal moment calculations from the bulk apparent conductivity measurements (Fig. 4E-H) have similar trends and values as the above-logjam calculations. Between the logjam sites, the skew and therefore the interpreted retention at the above- and below-logjam locations were similar for the first two of our tracer tests.

### 3.5. *Logjam models*

At high or low flows, the BTC 1 m below the stream (at Y = 15 m, Z = 2 m) for the logjam models has a similar shape and magnitude to the corresponding no-jam models (Fig. 6A-C). In other words, the jam does not lead to strong heterogeneity in shallow solute transport 1 m below the stream. The mean arrival times are relatively similar for the high- and low-flow models at all three transects (Fig. 7A-B). At both high and low flow, the variance and skew increase from above the logjam to below it (Transects A to B) but decrease from below the logjam into the control transect (Transects B to C) (Fig. 7C-D), although values are small.

The concentration at 2 m below the stream (at Y = 15 m, Z = 3 m) is much more sensitive to the existence of a jam, and the BTCs vary with distance downstream (Fig. 6D-F). Enough mass was detected 2 m below the stream in the two logjam models to calculate the higher temporal moments, unlike the no-logjam models (Fig. 7F-H), which serves as one indication of the logjam's ability to increase the extent of tracer movement into the subsurface. The low-flow, logjam model did not have enough detected at Transect C to calculate meaningful moments, although the high-flow, logjam model did, which suggests the higher flows keep the tracer in the subsurface farther downstream. The high-flow, logjam model's skew at Transect C (Fig. 7H) is also negative here, interestingly, due to a secondary peak in concentration (Fig. 8), which we also observe 2 m lateral to the stream.

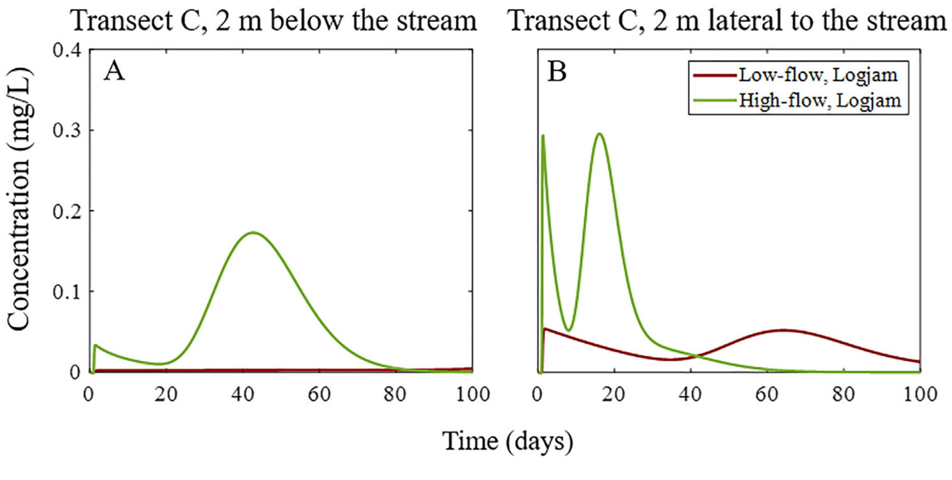

**Fig. 8.** Comparison of the concentration 2 m below the stream and 2 m lateral to the stream for the logjam, high-flow model and the logjam, low-flow model at Transect C, the control (X = 50 m), showing a secondary peak. The cell 2 m below the stream for the logjam, low-flow model shows that the concentration in that cell remained close to zero for the entire period.

The cell located 2 m lateral to the stream (at Y = 13 m, Z = 1 m) also shows a higher sensitivity to the presence of a logjam at both high and low flows compared to the cell 1 m below the stream (Fig. 6I-L). While the two logjam models had a higher observed tracer mass 2 m lateral to the stream compared to the no-logjam models, similar patterns in mean arrival time, variance, and skew for Transects A and B exist (Fig. 7I-L). At Transect C, the control transect, we see differences between the logjam and no-logjam models, especially the negative skew for the low-flow, logjam model (Fig. 7L) due to the secondary peak in concentration 2 m lateral to the stream driven by the logjam (Fig. 8). The logjam drives the tracer deeper into the subsurface, and the tracer travels downgradient at a slower velocity than solute in the stream, causing two peaks in concentration associated with rapid dispersion from the stream and slow advection along deeper flow paths (Figure SI-5). At high flow, the skew is positive at Transect C, the downstream control; however, it is not as large as it would be because of the second peak (Fig. 7L and 8).

The two logjam models are both losing streams but have localized zones of upwelling that the no-logjam models lack. The low-flow scenario is a losing stream with $3 \times 10^{-5}$ m$^3$/s entering the subsurface and $1 \times 10^{-5}$ m$^3$/s returning to the stream (Table 3). The $1 \times 10^{-5}$ m$^3$/s returning flow represents HEF occurring in this model, which is created by the logjam (no return flow occurs in scenarios without a jam). The high-flow, logjam model has the largest rate of flow from stream to aquifer, $1 \times 10^{-4}$ m$^3$/s, and the highest HEF, $5 \times 10^{-5}$ m$^3$/s, compared to the three other models (Table 3).

## 4. Discussion

Three important inferences can be made from our field measurements and numerical models: 1) logjams increase the extent and amount of the tracer movement into the subsurface, 2) logjams create complex transport pathways that can lead to bimodal BTC behavior, and 3) higher flow increases the extent of HEF. These interpretations are discussed in detail below, first in relation to the field measurements and then model results. The models generally agree with findings from the field and provide further insight into hyporheic processes happening in the field, as described below; we also outline differences between field data and generalized numerical models.

### 4.1. Jams increase the extent and amount of HEF

The ER imaging from the three transects in the field provide an illuminating look at hyporheic processes. Comparing the above-logjam ER images (Fig. 5E, SI-1E, SI-2E) to the below-logjam (Fig. 5F, SI-1F, SI-2F) and control ER images (Fig. 5D, SI-1D, SI-2D), the tracer moves deeper into the subsurface and further laterally from the stream above the jam. While there are many geologic and hydrologic complexities that can alter hyporheic flow paths, the above- and below-logjam transects are only a few meters apart and therefore are as similar in terms of geology, vegetation, and slope as we could hope for in the field. The crucial difference between them is the logjam. The above-logjam transect experiences the increased hydraulic resistance from the jam, which causes pooling and higher amounts of downwelling. Based on this, we conclude that the higher extent of the HEFs both vertically and horizontally in the above-logjam ER images (Fig. 5E, SI-1E, SI-2E) are a direct result of the logjam, because the below-logjam ER images (Fig. 5F, SI-1F, SI-2F) show the tracer only directly under the stream. While the other hydraulic conditions influence the shape or paths of the larger HEFs, the stark contrast between the above- and below-logjam ER images shows the impact a logjam can have on the amount and extent of groundwater-surface water exchange.

Our ER images show us the affect a logjam has on increasing HEF extent, but we can also infer the factors that control the shape or paths of enlarged HEFs. Near-stream vegetation and streambank slope likely influence HEF, and their affects can be seen in our ER images. For example, the tracer at the control transect moves underneath the streambed and into the left bank (Fig. 5D, SI-1D and SI-2D), potentially due to the lower slope and high density of vegetation on the left bank. The vegetation could induce flow away from the stream as well as create more porosity around roots, which would cause HEF to favor that bank (e.g., Menichino et al., 2014). Similarly, the tracer at the above-logjam transect moves mostly through the right bank of the stream (Fig. 5E, SI-1E and SI-2E), but to a greater extent than the control. The right bank at the logjam was highly vegetated, had a lower slope, and had standing water during high flows. The standing water suggests that the water table is near the surface, allowing easy exchange of water through thick, saturated sediments. The steepness of the left bank could also indicate bedrock at shallower depths and therefore lower hydraulic conductivity of the subsurface material. Bedrock geometry and valley constraint have been shown to influence hyporheic transport behavior in similar streams (e.g., Ward et al., 2016). The ER images and the variations among the three transects demonstrate the complexity of groundwater-surface water exchange processes and reinforce the importance of logjams. While our ER images provide a qualitative look at hyporheic processes, temporal moments let us gauge differences between the transects more quantitatively. Calculated skew was greater for the fluid and mean bulk apparent conductivity at both logjam transects compared to the control (Fig. 4D and H), which is interpreted as higher retention; the logjam transects show a much slower return to background when compared to the rapid decrease seen in the control. Our ER measurements and skew calculations support the observations from the ER images and show that the logjam increases HEF.

In terms of logjams increasing the extent and amount of HEF, the model results show: tracer downwelling (Figure SI-5), larger calculated skew values farther from the stream (at 2 m deep and 2 m lateral from it; Fig. 7H and L), and the existence of upwelling return flows in the logjam models (Table 3). The model lacks the inherent heterogeneity in the field and thus cannot account for all effects since in the field, but it does show deeper and wider exchange around the logjam. Figure SI-5 provides a cross-sectional view of the tracer through time in the subsurface for all four models, and the greater depth of tracer movement above the logjam at the two different flow rates is distinct. This result, as well as the higher amounts of tracer 2 m below and lateral to the stream in the logjam vs no-logjam models, provide evidence of the increased extent of HEF from a logjam. The same observations were made about the logjam in the field: the largest HEF extent was observed above the logjam (Fig. 5E). This correlates with the large downwelling above the logjam in the model. Similarly, Wondzell et al. (2009) observed downwelling upstream of major slope breaks, such as those associated with logjams, and upwelling downstream of these features, and Sawyer and Cardenas (2012) showed that adding logs created upwelling zones in an otherwise losing stream. From the model, we see that the logjam not only drives changes in HEF immediately around it but also farther downstream.

### 4.2. Higher flows increase HEF around jams

We find that higher flows increase the amount and extent of HEF. The ER images from the June test show the largest hyporheic area (based on the ≥ 200% change in bulk conductivity contour; Fig. 5D-F) compared to the two July tests which were at lower flow (Figure SI-1D-F and SI-2D-F). The model, even with a lack of heterogeneity, also shows the tracer moving deeper and wider during the high flow scenario (Figure SI-5G-L). The deeper flow paths and higher change in bulk conductivity imaged by the ER in June when compared to July suggest that higher flows increase the extent of HEF, but not necessarily the time water spends in the subsurface. The mean arrival times are as long or longer at each transect for the lower stream flows compared to the higher flow (Fig. 4B and F), which is expected in terms of transport velocity in the stream (Jobson, 2002) and its impact on flows in the subsurface. At low flows, the longer mean arrival times indicate that water moves through the smaller hyporheic zone more slowly.

Skew appears to decrease with flow in the field, although there are differences between the July 10–11 and July 28–29 tests despite similar flows ($Q = 0.17$ and $0.18\ m^3/s$, respectively; Fig. 4D and H); this could be due to gaps in the data due to thunderstorms (see Section 4.4, which outlines limitations of this study). Regardless, both July tests have lower skew values than the high-flow test in June. While this suggests larger tailing in the lower flows in June, we know that our ER data are truncated for all three tracer tests due to limitations in the field that prohibited additional observations. Therefore, the relationship between flows and retention (skew) values could be different than indicated by our calculations.

The modeling results also show that higher flows increase the extent of HEF. The tracer was observed 4 m deep in the logjam, high-flow model two days after the injection ended, while the logjam, low-flow model only detected the tracer to 3 m deep at the same time after the tracer test. The tracer was also observed 6 m lateral to the stream two days after the end of injection for the logjam, high-flow model, while the logjam, low-flow only observed tracer 4 m lateral to the stream at the same time. There was also a greater amount of calculated HEF in the high-flow, logjam model compared to the low-flow, logjam model (Table 3). These results support our field observations, which show an increase in HEF extent under high flows, particularly when comparing the varying flows at the transect immediately above the jam. The above-logjam transect from the high-flow tracer test in June (Fig. 5E) shows deeper flow paths, and larger lateral extent (again, based on the 200% change in bulk conductivity contour) compared to the corresponding transect at low flow (Figure SI-1E and SI-2E).

The numerical models also suggest that lower flows increase solute retention in streams, similar to other studies (e.g., Morrice et al., 1997), but this is not corroborated by the field measurements. The low-flow, logjam model exhibits increased tailing (consistently higher skew values) in comparison to the high-flow, logjam model in every cell at all transects except where concentrations were too low for moment calculations or the second peak caused a negative skew value (e.g., 2 m lateral to the stream at the simulated control, Transect C; Fig. 7D, H, L). While the model shows that lower flow increases retention times compared to the high flow, this was not clearly observed in the field measurements. On the contrary, slightly higher skew values were observed for the high flow tracer test (June 13–14) in the field compared to the two low flow tests (July 10–11 and July 28–29) (Fig. 4D, H). This is likely due to the truncation of the apparent bulk conductivity BTC discussed below.

### 4.3. Bimodal transport behavior

The mean bulk apparent conductivity at the control transect (Fig. 3A, SI-3A, and SI-4A) shows a secondary peak after the tracer ends for all three tracer tests that is not observed at the two logjam sites. This secondary peak is also observed downstream of the logjam (Transect C) in the numerical models with a simulated logjam (Fig. 8). The secondary peak is likely an effect of the control transect being downstream of the logjam site and the slow movement of tracer through the subsurface, and causes the skew values to be lower at the control site than would otherwise be expected, because the rising limb of the second peak creates negative moments in the calculation.

The observed secondary peak is one of the most interesting similarities between the field measurements and the numerical model results. Using only field measurements, the exact cause of the secondary peak is unclear, but because this phenomenon was also observed in our models, it is easier to interpret what may have caused the bimodal BTCs in the field. The secondary peak only occurs in the logjam models, and the tracer remains in the subsurface between the area above the logjam near Transect A to the region below Transect C. Therefore, we can infer that the secondary peak in the field data at the control is driven by tracer remaining in the subsurface from downwelling above the logjam. Similar observations of a secondary peak in tracer concentration have been seen in other studies (Toran et al, 2013; Sawyer et al., 2015). This secondary peak demonstrates that hyporheic flows induced by the logjam remain in the subsurface for a substantial amount of time and travel distance; this increase in HEF residence times and extent may be a primary driver in reaction rates for nutrients such as nitrates (e.g., Triska et al., 1989; Briggs et al., 2014). The secondary peak also explains why the skew value is lower at the control site and at Transect C compared to the upstream transects (Fig. 4D, H and Fig. 7D, H, L); the secondary peak introduces a left or negative skew in the calculation.

### 4.4. Limitations of this study

While we attempted to identify two experimental reaches where the primary difference was the presence or absence of a logjam, this is a natural stream with substantial spatial heterogeneity. Consequently, there are undoubtedly differences in alluvial sediment width, depth, porosity, and permeability between the logjam and control sites that influence the results in ways that are difficult to isolate or measure in fine detail. The control site is also downstream of the logjam site—the only feasible option for these experiments due to the existence of logjams upstream—which led to additional complications since the control site was influenced by the upstream hydrologic processes at the logjam.

One other issue was truncation of data in the field due to limitations on human resources and unexpected weather. Although the correlation between increased retention times and lower flows was shown by the model, the field data do not definitively support this result. However, if the ER surveys in the field were run for longer and thus were not truncated, the field results may have been more similar to the model results. This issue of truncation was tested in the model; stopping the monitoring period early, one day after the end of the tracer injection, resulted in lower or sometimes negative skew values, more similarly matching the data from the field. Another complication in our analyses is that there were thunderstorms throughout the day on July 28, including heavy rain and lightning; the former undoubtedly altered the fluid and bulk apparent conductivity, and the latter forced us to halt ER monitoring. Consequently, we lost data during the tracer injection and within a few hours after the injection stopped. The biggest gap in data is between 1553 and 1912 hr; the end of this data gap is where the large secondary peak in the control reach occurs.

### 4.5. Implications

ER provides valuable information on the relative extent of HEF, which is an improvement over point measurements in-stream, especially in sites with thin alluvial cover where installing samplers is challenging. Because ER methods can be time intensive and require a high initial cost, however, ER is not a long-term monitoring method for all restoration efforts. That said, it can be used to further research in restoration, and the results from the ER measurements could also provide a basis for more practical long-term monitoring methods, such as measuring stream temperature and head drops across structures like logjams. River management operations, such as adding large wood in streams, commonly involve strategies to offset negative impacts that occurred from controlling and engineering stream systems or altering land use. Current river management and restoration practices that incorporate large wood placement typically use few quantitative or predictive methods for implementation. Advancing the predictive and quantitative basis for using large wood and logjams for restoration requires characterizing the relation between logjams and hyporheic exchange rates, and this work offers a possible framework for assessment.

## 5. Conclusions

Our field measurements and numerical models support the conclusion that logjams increase HEF. Longer tailing, as quantified by the temporal moment skew, is observed in both the field measurements and numerical modeling results for reaches with logjams compared to those without. Logjams also create complex flow paths in the subsurface and can result in bimodal BTCs, which is seen downstream of the logjam in both the model and field BTCs. Furthermore, higher flows increase the depth and lateral extent of HEF paths, particularly around logjams. In the models, substantially more tracer mass is detected at greater depth and lateral distance in the logjam model scenarios under high-flow. In ER inversions, a larger HEF extent is observed during high flow above the logjam. Lower flows have a smaller extent of HEF and they decrease the flow in the hyporheic zone, possibly resulting in longer residence times. While models show higher retention or skew at low-flows, field observations on the relationship between flow rate and retention are less conclusive, perhaps due to data truncation. These findings may be used to advance stream restoration and conservation efforts, providing a foundation for placing wood or engineered logjams into streams.

## CRediT authorship contribution statement

**M. Doughty:** Data curation, Formal analysis, Funding acquisition, Investigation, Methodology, Project administration, Resources, Software, Visualization, Writing - original draft. **A.H. Sawyer:** Conceptualization, Formal analysis, Funding acquisition, Methodology, Validation, Writing - review & editing. **E. Wohl:** Conceptualization, Funding acquisition, Investigation, Methodology, Resources, Writing - review & editing. **K. Singha:** Conceptualization, Formal analysis, Funding acquisition, Investigation, Methodology, Project administration, Resources, Supervision, Validation, Writing - review & editing.

## Declaration of Competing Interest

The authors declare that they have no known competing financial interests or personal relationships that could have appeared to influence the work reported in this paper.

## Acknowledgements

This research was supported by the National Science Foundation (award no. EAR-1819134) the Geological Society of America, and a Colorado School of Mines Mann Research Grant. We would like to give a big thank you for all those who assisted in field work: Jackie Randell, Ethan Ader, Teodora Mitroi, James Proctor, Emily Iskin, Amelia Nelson, and Kenny Swift Bird. We also appreciate the feedback from our reviewers and the associate editor. The data and models from this paper have been published on CUAHSI's HydroShare at https://www.hydroshare.org/resource/e12778e5718b414ab530381e89bf24ed/.

## Appendix A. Supplementary data

Supplementary data to this article can be found online at https://doi.org/10.1016/j.jhydrol.2020.124931.

## References

Ader, E. (2019). Geomorphic Effects of Increased Wood Loading on Hyporheic Exchange Flow. Unpublished MS Thesis.

Allan, J.D., 2004. Landscapes and riverscapes: the influence of land use on stream ecosystems. Ann. Rev. Ecol. Evolut. Systemat. https://doi.org/10.1146/annurev.ecolsys.35.120202.110122.

Anderson, J. K., Wondzell, S. M., Gooseff, M. N., & Haggerty, R. (2005). Patterns in stream longitudinal profiles and implications for hyporheic exchange flow at the H.J. Andrews Experimental Forest, Oregon, USA. Hydrol. Process. Doi: 10.1002/hyp.5791.

Ben Simon, R., Bernard, S., Meurville, C., Rebour, V., 2015. Flow-Through Stream Modeling with MODFLOW and MT3D: Certainties and Limitations. Groundwater. https://doi.org/10.1111/gwat.12312.

Bernhardt, E.S., Palmer, M.A., 2007. Restoring streams in an urbanizing world. Freshw. Biol. https://doi.org/10.1111/j.1365-2427.2006.01718.x.

Bethune, J., Randell, J., Runkel, R.L., Singha, K., 2015. Non-invasive flow path characterization in a mining-impacted wetland. J. Contam. Hydrol. https://doi.org/10.1016/j.jconhyd.2015.10.002.

Binley, A., Kemna, A., 2005. DC resistivity and induced polarization methods BT - Hydrogeophysics. Hydrogeophysics.

Briggs, M.A., Lautz, L.K., Hare, D.K., 2014. Residence time control on hot moments of net nitrate production and uptake in the hyporheic zone. Hydrol. Process. https://doi.org/10.1002/hyp.9921.

Buffington, J.M., Tonina, D., 2009. Hyporheic exchange in mountain rivers II: Effects of channel morphology on mechanics, scales, and rates of exchange. Geography Compass. https://doi.org/10.1111/j.1749-8198.2009.00225.x.

Campbell, I.C., Doeg, T.J., 1989. Impact of timber harvesting and production on streams: A review. Mar. Freshw. Res. https://doi.org/10.1071/MF9890519.

Cardenas, M.B., Markowski, M.S., 2011. Geoelectrical imaging of hyporheic exchange and mixing of river water and groundwater in a large regulated river. Environ. Sci. Technol. https://doi.org/10.1021/es103438a.

Cardenas, M.B., Wilson, J.L., Zlotnik, V.A., 2004. Impact of heterogeneity, bed forms, and stream curvature on subchannel hyporheic exchange. Water Resour. Res. https://doi.org/10.1029/2004WR003008.

Coscia, I., Greenhalgh, S.A., Linde, N., Doetsch, J., Marescot, L., Gu, T., Green, A.G., 2011. 3D crosshole ERT for aquifer characterization and monitoring of infiltrating river water. Geophysics. doi 10 (1190/1), 3553003.

Drummond, J.D., Covino, T.P., Aubeneau, A.F., Leong, D., Patil, S., Schumer, R., Packman, A.I., 2012. Effects of solute breakthrough curve tail truncation on residence time estimates: A synthesis of solute tracer injection studies. *Journal of Geophysical Research.* Biogeosciences. https://doi.org/10.1029/2012JG002019.

Endreny, T., Lautz, L., Siegel, D.I., 2011. Hyporheic flow path response to hydraulic jumps at river steps: Flume and hydrodynamic models. Water Resour. Res. https://doi.org/10.1029/2009WR008631.

Fanelli, R.M., Lautz, L.K., 2008. Patterns of water, heat, and solute flux through streambeds around small dams. Ground Water. https://doi.org/10.1111/j.1745-6584.2008.00461.x.

Gooseff, M. N., Anderson, J. K., Wondzell, S. M., LaNier, J., & Haggerty, R. (2006). A modelling study of hyporheic exchange pattern and the sequence, size, and spacing of stream bedforms in mountain stream networks, Oregon, USA. Hydrol. Process. doi: 10.1002/hyp.6349.

Gupta, A., Cvetkovic, V., 2000. Temporal moment analysis of tracer discharge in streams: Combined effect of physicochemical mass transfer and morphology. Water Resour. Res. https://doi.org/10.1029/2000WR900190.

Hancock, P.J., 2002. Human impacts on the stream-groundwater exchange zone. Environ. Manage. https://doi.org/10.1007/s00267-001-0064-5.

Harbaugh, Arlen, W. (2005). MODFLOW-2005 , The U . S . Geological Survey Modular Ground-Water Model — the Ground-Water Flow Process. U.S. Geological Survey Techniques and Methods. https://doi.org/U.S. Geological Survey Techniques and Methods 6-A16.

Harvey, C.F., Gorelick, S.M., 1995. Temporal Moment-Generating Equations: Modeling Transport and Mass Transfer in Heterogeneous Aquifers. Water Resour. Res. https://doi.org/10.1029/95WR01231.

Harvey, J.W., Bencala, K.E., 1993. The Effect of streambed topography on surface-subsurface water exchange in mountain catchments. Water Resour. Res. https://doi.org/10.1029/92WR01960.

Hayley, K., Bentley, L.R., Gharibi, M., Nightingale, M., 2007. Low temperature dependence of electrical resistivity: Implications for near surface geophysical monitoring. Geophys. Res. Lett. https://doi.org/10.1029/2007GL031124.

Hayley, K., Bentley, L.R., Pidlisecky, A., 2010. Compensating for temperature variations in time-lapse electrical resistivity difference imaging. Geophysics 10 (1190/1), 3478208.

Hester, E.T., Doyle, M.W., 2008. In-stream geomorphic structures as drivers of hyporheic exchange. Water Resour. Res. https://doi.org/10.1029/2006WR005810.

Jackson, K.J., & Wohl, E. (2015). Instream wood loads in montane forest streams of the Colorado Front Range, USA. Geomorphology. Do: i10.1016/j.geomorph.2015.01.022.

Jobson, H.E., 2002. Predicting Travel Time and Dispersion in Rivers and Streams. J. Hydraul. Eng. https://doi.org/10.1061/(asce)0733-9429(1997)123:11(971).

Kail, J., Hering, D., Muhar, S., Gerhard, M., Preis, S., 2007. The use of large wood in stream restoration: Experiences from 50 projects in Germany and Austria. J. Appl. Ecol. https://doi.org/10.1111/j.1365-2664.2007.01401.x.

Keller, G.V., Frischknecht, F.C., 1966. Electrical Methods in Geophysical Prospecting. Pergamon Press, Oxford.

LaBrecque, D.J., Yang, X., 2009. Difference Inversion of ERT Data: a Fast Inversion Method for 3-D In Situ Monitoring. J. Environ. Eng. Geophys. https://doi.org/10.4133/jeeg6.2.83.

Lautz, L.K., Siegel, D.I., Bauer, R.L., 2006. Impact of debris dams on hyporheic interaction along a semi-arid stream. Hydrol. Process. https://doi.org/10.1002/hyp.5910.

Livers, B., Wohl, E., 2016. Sources and interpretation of channel complexity in forested subalpine streams of the Southern Rocky Mountains. Water Resour. Res. https://doi.org/10.1002/2015WR018306.

Loheide, S.P., Lundquist, J.D., 2009. Snowmelt-induced diel fluxes through the hyporheic zone. Water Resour. Res. 45 (7).

Manners, R.B., Doyle, M.W., Small, M.J., 2007. Structure and hydraulics of natural woody debris jams. Water Resour. Res. https://doi.org/10.1029/2006WR004910.

Mao, X., Enot, P., Barry, D.A., Li, L., Binley, A., Jeng, D.S., 2006. Tidal influence on behaviour of a coastal aquifer adjacent to a low-relief estuary. J. Hydrol. https://doi.org/10.1016/j.jhydrol.2005.11.030.

Menichino, G.T., Ward, A.S., Hester, E.T., 2014. Macropores as preferential flow paths in meander bends. Hydrol. Process. https://doi.org/10.1002/hyp.9573.

Millington, C.E., Sear, D.A., 2007. Impacts of river restoration on small-wood dynamics in a low-gradient headwater stream. Earth Surf. Proc. Land. https://doi.org/10.1002/esp.1552.

Morrice, J.A., Valett, H.M., Dahm, C.N., Campana, M.E., 1997. Alluvial characteristics, groundwater-surface water exchange and hydrological retention in headwater streams. Hydrol. Process. https://doi.org/10.1002/(SICI)1099-1085(19970315)11:3<253::AID-HYP439>3.0.CO;2-J.

Nakamura, F., Swanson, F.J., 1993. Effects of coarse woody debris on morphology and sediment storage of a mountain stream system in western Oregon. Earth Surf. Proc. Land. https://doi.org/10.1002/esp.3290180104.

Palmer, M.A., Menninger, H.L., Bernhardt, E., 2010. River restoration, habitat heterogeneity and biodiversity: A failure of theory or practice? Freshw. Biol. https://doi.org/10.1111/j.1365-2427.2009.02372.x.

Payn, R. A., Gooseff, M. N., McGlynn, B. L., Bencala, K. E., & Wondzell, S. M. (2009). Channel water balance and exchange with subsurface flow along a mountain headwater stream in Montana, United States. Water Res. Res. doi: 10.1029/2008WR007644.

Poff, N.L., Olden, J.D., Merritt, D.M., Pepin, D.M., 2007. Homogenization of regional river dynamics by dams and global biodiversity implications. Proceed. Natl. Acad. Sci. https://doi.org/10.1073/pnas.0609812104.

Robinson, C., Li, L., Barry, D.A., 2007. Effect of tidal forcing on a subterranean estuary. Adv. Water Resour. https://doi.org/10.1016/j.advwatres.2006.07.006.

Roni, P., Beechie, T., Pess, G., Hanson, K., 2014. Wood placement in river restoration: fact, fiction, and future direction. Can. J. Fish. Aquat. Sci. https://doi.org/10.1139/cjfas-2014-0344.

Salehin, M., Packman, A.I., Paradis, M., 2004. Hyporheic exchange with heterogeneous streambeds: Laboratory experiments and modeling. Water Resour. Res. https://doi.org/10.1029/2003WR002567.

Sawyer, A.H., Bayani Cardenas, M., Buttles, J., 2011. Hyporheic exchange due to channel-spanning logs. Water Resour. Res. https://doi.org/10.1029/2011WR010484.

Sawyer, A.H., Bayani Cardenas, M., Buttles, J., 2012. Hyporheic temperature dynamics and heat exchange near channel-spanning logs. Water Resour. Res. https://doi.org/10.1029/2011WR011200.

Sawyer, A.H., Cardenas, M.B., 2012. Effect of experimental wood addition on hyporheic exchange and thermal dynamics in a losing meadow stream. Water Resour. Res. https://doi.org/10.1029/2011WR011776.

Sawyer, A.H., Zhu, J., Currens, J.C., Atcher, C., Binley, A., 2015. Time-lapse electrical resistivity imaging of solute transport in a karst conduit. Hydrol. Process. https://doi.org/10.1002/hyp.10622.

Sear, D.A., Millington, C.E., Kitts, D.R., Jeffries, R., 2010. Logjam controls on channel:-floodplain interactions in wooded catchments and their role in the formation of multi-channel patterns. Geomorphology. https://doi.org/10.1016/j.geomorph.2009.11.022.

Sedell, J. R., Leone, F. N., & Duval, W. S. (1991). Water transportation and storage of logs. American Fisheries Society Special Publication 19.

Singha, K., Pidlisecky, A., Day-Lewis, F.D., Gooseff, M.N., 2010. Electrical characterization of non-Fickian transport in groundwater and hyporheic systems. Water Resour. Res. https://doi.org/10.1029/2008WR007048.

Slater, L. D., Ntarlagiannis, D., Day-Lewis, F. D., Mwakanyamale, K., Versteeg, R. J., Ward, A., … Lane, J. W. (2010). Use of electrical imaging and distributed temperature sensing methods to characterize surface water-groundwater exchange regulating uranium transport at the Hanford 300 Area, Washington. Water Resour. Res. Doi: 10.1029/2010WR009110.

Sweeney, B.W., Newbold, J.D., 2014. Streamside forest buffer width needed to protect stream water quality, habitat, and organisms: A literature review. J. Am. Water Resour. Assoc. https://doi.org/10.1111/jawr.12203.

Tonina, D., Buffington, J.M., 2007. Hyporheic exchange in gravel bed rivers with pool-riffle morphology: Laboratory experiments and three-dimensional modeling. Water Resour. Res. https://doi.org/10.1029/2005WR004328.

Tonina, D., Buffington, J.M., 2009. Hyporheic exchange in mountain rivers I: Mechanics and environmental effects. Geograp. Compass. https://doi.org/10.1111/j.1749-8198.2009.00226.x.

Tonina, D., Buffington, J.M., 2011. Effects of stream discharge, alluvial depth and bar amplitude on hyporheic flow in pool-riffle channels. Water Resour. Res. https://doi.org/10.1029/2010WR009140.

Toran, L., Hughes, B., Nyquist, J., Ryan, R., 2012. Using hydrogeophysics to monitor change in hyporheic flow around stream restoration structures. Environ. Eng. Geosci. https://doi.org/10.2113/gseegeosci.18.1.83.

Toran, L., Nyquist, J. E., Fang, A. C., Ryan, R. J., & Rosenberry, D. O. (2013a). Observing lingering hyporheic storage using electrical resistivity: Variations around stream restoration structures, Crabby Creek, PA. Hydrol. Process. Doi: 10.1002/hyp.9269.

Triska, F.J., Kennedy, V.C., Avanzino, R.J., Zellweger, G.W., Bencala, K.E., 1989. Retention and transport of nutrients in a third-order stream in northwestern California; hyporheic processes. Ecology. https://doi.org/10.2307/1938120.

Ward, A.S., Gooseff, M.N., Fitzgerald, M., Voltz, T.J., Singha, K., 2014. Spatially distributed characterization of hyporheic solute transport during baseflow recession in a headwater mountain stream using electrical geophysical imaging. J. Hydrol. https://doi.org/10.1016/j.jhydrol.2014.05.036.

Ward, A.S., Gooseff, M.N., Singha, K., 2010a. Characterizing hyporheic transport processes - Interpretation of electrical geophysical data in coupled stream-hyporheic zone systems during solute tracer studies. Adv. Water Resour. https://doi.org/10.1016/j.advwatres.2010.05.008.

Ward, A.S., Gooseff, M.N., Singha, K., 2010b. Imaging hyporheic zone solute transport using electrical resistivity. Hydrol. Process. https://doi.org/10.1002/hyp.7672.

Ward, A.S., Schmadel, N.M., Wondzell, S.M., Harman, C., Gooseff, M.N., Singha, K., 2016. Hydrogeomorphic controls on hyporheic and riparian transport in two headwater mountain streams during base flow recession. Water Resour. Res. https://doi.org/10.1002/2015WR018225.

Wohl, E., 2005. Compromised rivers: Understanding historical human impacts on rivers in the context of restoration. Ecol. Soc. https://doi.org/10.5751/ES-01339-100202.

Wohl, E., 2006. Human impacts to mountain streams. Geomorphology. https://doi.org/10.1016/j.geomorph.2006.06.020.

Wohl, E., Beckman, N.D., 2014. Leaky rivers: Implications of the loss of longitudinal fluvial disconnectivity in headwater streams. Geomorphology. https://doi.org/10.1016/j.geomorph.2011.10.022.

Wondzell, S. M. (2006). Effect of morphology and discharge on hyporheic exchange flows in two small streams in the Cascade Mountains of Oregon, USA. Hydrol. Processes. Doi: 10.1002/hyp.5902.

Wörman, A., Packman, A.I., Johansson, H., Jonsson, K., 2002. Effect of flow-induced exchange in hyporheic zones on longitudinal transport of solutes in streams and rivers. Water Resour. Res. https://doi.org/10.1029/2001WR000769.

Wroblicky, G.J., Campana, M.E., Valett, H.M., Dahm, C.N., 1998. Seasonal variation in surface-subsurface water exchange and lateral hyporheic area of two stream-aquifer systems. Water Resour. Res. https://doi.org/10.1029/97WR03285.

Zheng, C., Wang, P.P., 1999. MT3DMS: a modular three-dimensional multispecies transport model for simulation of advection, dispersion, and chemical reactions of contaminants in groundwater systems; documentation and user's guide. Alabama Univ University.